A New Relieving-DC-Saturation Hybrid Excitation Vernier Machine for HEV Starter Generator Application

Xing Zhao, Shuangxia Niu *IEEE Senior Member,* Xiaodong Zhang, Weinong Fu

Abstract—Benefiting from flexible flux control and short-circuit withstand ability, hybrid excitation machine is an emerging starter generator solution for hybrid electric vehicle propulsion. However, to realize a brushless hybrid design in conventional PM machines, a three-dimensional magnetic circuit is usually adopted, leading to complicated mechanical structure and torque density sacrifice. To address this issue, a new relieving-DC-saturation hybrid excitation Vernier machine is proposed in this paper, which integrates good torque density and bidirectional flux control within a simple and brushless structure. The key is to artificially construct reluctance effect in a consequent-pole Vernier PM machine (CP-VPMM) by introducing extra DC field excitation equipped with relieving-DC-saturation ability. In this way, the advantages of bidirectional flux control in stator-DC-excited reluctance machine and good torque density in CP-VPMM are well combined in this topology, making it especially suitable for multi-mode starter generator application. In this paper, the machine structure and its design mechanism are introduced, with its electromagnetic performance evaluated by the finite element simulation. A prototype is manufactured and tested. Experiment results verify the feasibility of this new topology.

Index Terms—Brushless hybrid design, HEV starter generator, relieving-DC-saturation effect, Vernier PM machine.

I. INTRODUCTION

With the increasing concerns of environmental pollution and energy consumption, the powertrain electrification is the most popular trend to reduce the use of nonrenewable petroleum [1]. Full electric vehicles now still face challenges such as the limits of battery technology and charging pile popularization, thus not being fully widespread. Hence, hybrid electric vehicle (HEV), which combines the merits of engine and electrical powertrain, can be considered as an appropriate transitional solution.

Starter generator (SG) integrated design is an effective way to realize hybrid energy strategy for HEVs [2]. The SG solution presented in literature usually uses parallel architectures, which can be divided into two categories, namely the integrated starter generator (ISG) and belt-driven starter generator (BSG) [3-4]. ISG is inserted into the engine and needs a completely revised housing, while BSG as shown in Fig. 1, needs less modification of engine layout and thus becomes more cost-effective.

Electrical machine is the core of SG system and a variety of topologies have been studied and implemented as SG in HEVs. Induction machine (IM) is one of the popular SG candidates due to its low cost, robust structure, high overload ability and good flux weakening characteristic [5-7]. However, IM suffers from relatively low efficiency and power factor. Besides, its control strategy for wide-speed generation is complicated. Permanent magnet (PM) synchronous machine (PMSM) is an attractive SG
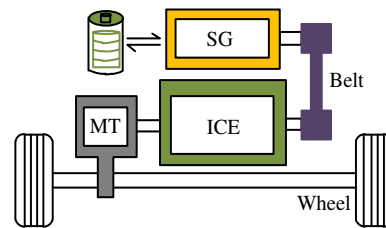
Fig. 1. Configuration of BSG system in HEV. (MT—mechanical transmission, ICE—internal combustion engine, SG—starter-generator).

However, PMSM has drawbacks such as high cost, poor flux weakening ability and thus limited constant power speed range. solution due to high torque density and high efficiency [8-10]. Switched reluctance machine (SRM) is another SG candidate, which owns the merits of low cost and high reliability [11-13]. However, SRM suffers from relatively low torque density [14]. Besides, the severe torque ripple in SRM results in implicative engine vibration [15], which is a critical issue in SG system.

Hybrid-excited machine (HEM) is another emerging solution for SG system [16-17]. Benefiting from the combination of PM excitation and wound field excitation, HEM has the advantages of good torque density, extended constant power speed range as well as wide-speed generation ability, making it suitable for the multi-mode SG operation in HEV. Many HEM topologies have been investigated in literature. According to the location of PM excitation, there are two typical layouts for HEMs. One design is with PMs placed at rotor side [18-20], namely rotor-PM HEM. Another design is with PMs at stator side [21-23], thus namely stator-PM HEM. A typical rotor-PM HEM is investigated as SG for aerospace propulsion [24]. It utilizes a magnetic-shunt rotor structure, in which the rotor core is extended in axial direction to artificially produce axial magnetic circuit for PMs. Besides, DC field coil is housed in the extended rotor cavity for magnetic field regulation. In this way, it realizes a brushless configuration. However, its mechanical structure becomes very complicated, which is not attractive for SG system considering the robustness and cost. Meanwhile, since the space for SG in HEV is limited, using magnetic-shunt rotor will lead to torque sacrifice. In [25], a typical stator-PM HEM SG is explored. It owns a simple and brushless structure. However, as a common issue in stator PM machines, its torque density is relatively disadvantages.

This paper aims to propose a new relieving-DC-saturation hybrid Vernier machine (RDCS-HVM) as SG candidate, which integrates good torque density and bidirectional flux regulation within a simple and brushless structure. This paper is organized as follows. In Section II, the machine structure and its operation mode as a SG is presented. In Section III, a theoretical analysis of design mechanism is performed. In Section IV, different slot pole combinations are compared. In Section V, the performance as a SG is evaluated by finite element analysis. In Section VI, the parameters analysis and design optimization are performed. In Section VII, a prototype is fabricated and fully tested. Then in Section VIII, a comparative discussion is performed. Finally, some conclusions are drawn in Section IX.

II. PROPOSED SG SYSTEM FOR HEV

A. Machine Construction

Fig. 2 presents the structure of the proposed RDCS-HVM for SG system, which consists of a 24-slot stator and a 22 pole-pair PM rotor. Both AC and DC coils are arranged in the stator slots. DC coils are identically wound to form a uniform DC excitation field, which is modulated by the rotor saliency effect to produce reluctance torque. Besides, the tangentially magnetized PMs are introduced into stator slots to relieve extra DC saturation effect caused by the constant DC flux component in stator core. The rotor adopts a consequent-pole structure, in which each PM and adjacent core constitute a pair of magnetic poles. All rotor PMs are magnetized in the same radial direction. The armature coils use a single-layer concentrated connection as shown in Fig. 3.

The features of the proposed topology can be listed as
(1) The machine structure is mechanically robust.
(2) Benefiting from a concentrated design, the winding ends are short, thus the copper loss and material cost are reduced.
(3) With unique relieving-DC-saturation design, the reluctance torque contribution can be boosted.
(4) The DC field terminal enables bidirectional field regulation, which gives flexible flux weakening and wide-speed generation operation. This is important for multi-mode SG operation.
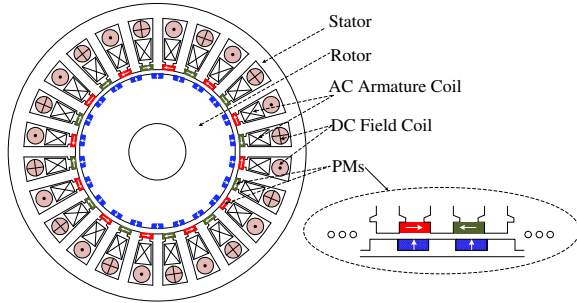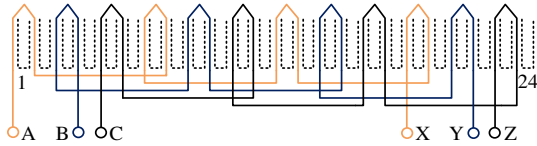

Fig. 2. Configuration of the proposed RDCS-HVM.

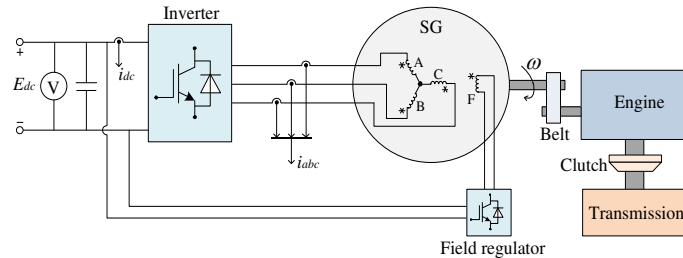Fig. 3. Connection of the armature winding.

Fig. 4. SG system based on the proposed RDCS-HVM.

B. Operation Modes as a SG in HEV

Based on the proposed RDCS-HVM, a SG system is built as presented in Fig. 4. As a SG for HEV, the proposed machine mainly has these three working modes, namely engine cranking, battery charging and torque overlapping, respectively.

Mode I, engine cranking. When an HEV stops for a long time and needs to start again, the SG should work as an electromotor

to drive the engine to the minimum operating speed. Therefore, the SG should have the ability to provide a continuous starting torque to overcome the drag force of a cold engine.

Mode II, battery charging. When the engine runs to a steady speed and takes charge of the propulsion, the SG should work as a generator and charge the battery until it is full. Meanwhile, if the HEV operates downhill or braked, the SG should perform regenerative braking and charge the battery.

Mode III, torque boosting. When the HEV operates under a low-speed climbing circumstance, the SG is required to perform as an electromotor to provide extra torque, which can assist the torque generated by the engine, and in such a way, the HEV can achieve a better climbing performance.

With extra DC field terminal in the proposed machine, more flexible SG control can be achieved at different HEV working conditions, which can be summarized as

At Mode I, by injecting positive maximum DC field current, boosted cranking torque can be achieved to shorten the start-up process of engine. Further, by coordinating DC field control and vector field control, enhanced flux weakening operation can be achieved, thus leading to extended constant power speed range.

At Mode II, by regulating the DC field excitation, the output voltage can be continuously adjusted to ensure smooth charging characteristic under different engine speed, which accordingly increase the service life of the rectifier and battery. Meanwhile, de-excitation operation can be performed when a power device short-circuit situation occurs, which can avoid the huge current strike and corresponding braking torque.

At Mode III, similar with that at Mode I, with a positive DC field current applied, enhanced assistant torque can be obtained, which gives the HEV an improved climbing-performance.

In general, the existence of DC field terminal in the proposed RDCS-HVM enables a more flexible torque and speed control at starting mode and wide voltage regulation at generation mode, thus it can be a potential SG candidate for HEVs.
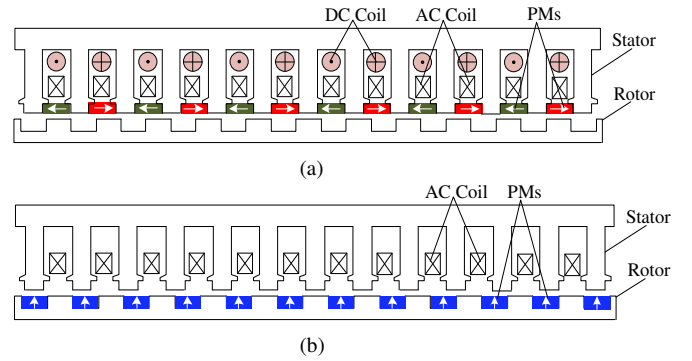
Fig. 5. Separation of the proposed RDCS-HVM. (a) RDCS-RM. (b) CP-VPMM.

III. DESIGN MECHANISM

Considering the parallel magnetic circuit excited by DC field coils and rotor PMs, the design principle of this new topology is explained by splitting it into two separate structures, namely relieving-DC-saturation reluctance machine (RDCS-RM) and consequent-pole Vernier PM machine (CP-VPMM), as denoted in Fig. 5. In the following part, the operation principles of two different structures will be introduced, and then their coupling relationship at no-saturation condition will be revealed to show the design mechanism of the proposed RDCS-HVM.

A. Relieving-DC-Saturation Reluctance Machine

Fig. 6 gives the flux distribution with rotor position variation in RDCS-RM. As denoted in Fig. 6(a), when the rotor salient pole is aligned with wound stator tooth, the loop reluctance for DC field excitation is minimized. Therefore, the coil flux of DC field source reaches the maximum value. In contrast, as shown in Fig. 6(b), when the rotor rotates half of pole pitch, the wound stator tooth is now aligned with the rotor slot, and consequently, the loop reluctance for DC field excitation is maximized and the coil flux now reaches the minimum value. As shown in Fig. 7(a), with the rotor rotation, a pulsating coil flux is produced by DC field excitation, which enables reluctance torque generation.

Moreover, PMs are introduced in stator slots to mitigate extra DC saturation effect in stator core caused by biased flux feature of DC field excitation. Specially, as shown in Fig. 6, regardless of the rotor positions, slot PMs link the stator core all the time due to the minimum reluctance principle and this constant PM bias is opposite against the DC flux bias of DC field excitation. Therefore, with slot PMs increasing, DC flux bias can decrease to zero as shown in Fig. 7(b), and thus the stator DC saturation can be eliminated to boost reluctance torque generation.
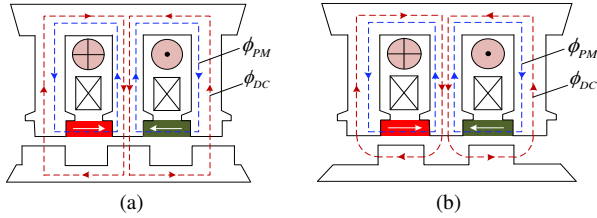

Fig. 6. Illustration of coil flux variation in RDCS-RM. (a) Position a, maximum DC flux. (a) Position b, minimum DC flux.
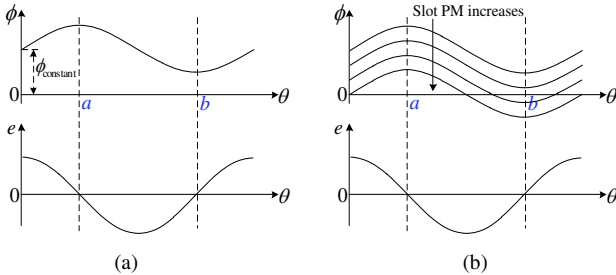

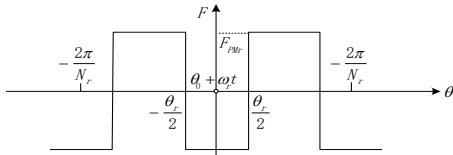Fig. 7. Coil flux and back EMF. (a) Without slot PMs. (b) With slot PMs
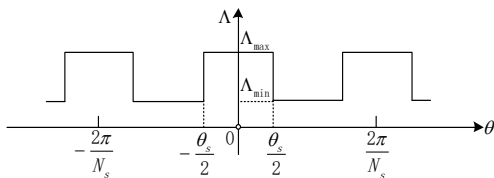

Fig. 8. MMF generated by rotor PMs.

Fig. 9. Permeance distribution at the stator side

B. Consequent-Pole Vernier PM Machine

For CP-VPMM, all PMs are magnetized in the same radially outward direction. Each PM and its adjacent core form a pair of magnetic poles, and the magnetomotive force (MMF) produced by rotor PMs is illustrated in Fig. 8, which can be expressed as

$$F_{PM}(\theta,t) = \sum_{n=1,3,5\ldots}^{\infty} \frac{4F_{PM}}{n\pi}\sin(np_{PM}\frac{\theta_r}{2})\cos[np_{PM}(\theta-\theta_0-\omega_r t)] \quad (1)$$

where F_{PM} is the amplitude of PM MMF, p_{PM} is the pole pair number of rotor PMs. θ_r is the arc of rotor pole. θ is the rotor mechanical angle and θ_0 is its initial value. ω_r is the angular velocity of rotor. t is the running time.

Due to the open-slot design at stator side, stator permeance is not uniform as shown in Fig. 9, which can be expanded as

$$\Lambda_s(\theta) = \Lambda_{s0} + \sum_{k=1}^{\infty} \frac{\Lambda_{s1}}{k\pi}\sin(kN_s\frac{\theta_s}{2})\cos(kN_s\theta) \quad (2)$$

where Λ_{s0} and Λ_{s1} are the average value and peak to peak value of the stator permeance, respectively. N_s is the number of stator teeth. θ_s is the arc of stator teeth. Then, the air-gap field excited by rotor PMs can be derived by multiplying (1) and (2)

$$
\begin{cases}
B_{PM}(\theta,t) = F_{PM}(\theta,t)\Lambda_s(\theta) = \dfrac{4F_{PM}\Lambda_{s0}}{\pi}\sum_{n=1,3,5}^{\infty} C_n\sin[np_{PM}(\theta-\theta_0-\omega_r t)] \\[4pt]
\quad + \dfrac{2F_{PM}\Lambda_{s1}}{\pi^2}\sum_{n=1,3,5}^{\infty}\sum_{k=1}^{\infty} C_n C_k[\cos(\varepsilon_1)+\cos(\varepsilon_2)] \\[4pt]
C_n = \dfrac{1}{n}\sin(np_{PMr}\dfrac{\theta_r}{2}),\ C_k = \dfrac{1}{k}\sin(kN_s\dfrac{\theta_s}{2}) \\[4pt]
\varepsilon_1 = (np_{PM}-kN_s)\left[\theta+\dfrac{np_{PM}}{np_{PM}-kN_s}(\theta_0+\omega_r t)\right] \\[4pt]
\varepsilon_2 = (np_{PM}+kN_s)\left[\theta-\dfrac{np_{PM}}{np_{PM}+kN_s}(\theta_0+\omega_r t)\right]
\end{cases} \quad (3)
$$

TABLE I
Harmonics Components Excited by Rotor PMs

Group	Spatial order	Amplitude	Rotation velocity
I	np_{PM}	$\dfrac{4F_{PM}\Lambda_{s0}}{\pi}C_n$	$n\omega_r$
II	$\|np_{PM}-kN_s\|$	$\dfrac{2F_{PM}\Lambda_{s1}}{\pi^2}C_n C_k$	$\dfrac{-np_{PM}}{\|np_{PM}-kN_s\|}\omega_r$
III	$np_{PM}+kN_s$	$\dfrac{2F_{PM}\Lambda_{s1}}{\pi^2}C_n C_k$	$\dfrac{np_{PM}}{np_{PM}+kN_s}\omega_r$

Based on Eq. (3), the excited harmonics by rotor PMs are listed in Table I. The harmonics in Group I are generated by PM field without modulation effect, similar with that in PM synchronous machine. The harmonics in Group II and Group III are produced by stator teeth modulation. Those harmonics with the same pole pair number and the same rotation speed as that in the armature field, will interact effectively and make PM torque generation. Based on the flux modulation theory [25], the pole pair number of armature winding p_a, and the rotation velocity of armature field ω_a, can be expressed as

$$p_a = |p_{PM}-N_s|,\ \omega_a = G_r\omega_r \quad (4)$$

where G_r is the magnetic gearing ratio and equals to $\frac{p_{PM}}{p_a}$.

C. Magnetic Coupling between Two Structures

As analyzed above, RDCS-RM and CP-VPMM both exist in the proposed topology. To effectively integrate two structures, two necessary conditions should be satisfied as follows.
(1) The armature winding must use a single-layer concentrated design. This is because, compared to double-layer concentrated design or distributed design, armature field excited by a single-layer concentrated design has more air gap harmonics, and thus it can synchronously interact with DC field excitation and rotor PM excitation, which have different pole pair numbers.

(2) The main magnetic circuit for each structure should not be designed at saturation condition. This is because two structures share the common magnetic circuit in both stator core and rotor core. Once a structure is designed in close to the saturation point, the effectiveness of the other machine will not be distinct.

The maximum flux distribution for two structures are shown in Fig. 10. It reveals that two structures can obtain the maximum flux at the same d-axis position, which means, flux components in two structures are entirely in phase and can couple effectively without any inner flux cancellation or phase shift.
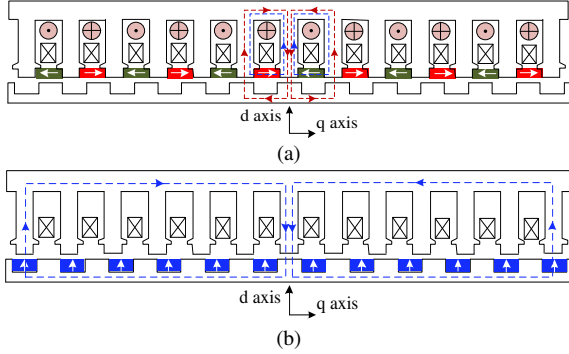

d axis   q axis

(a)

d axis   q axis

(b)

Fig. 10. D-axis flux for two structures. (a) RDCS-RM. (b) CP-VPMM.

IV. SELECTION OF SLOT/POLE COMBINATION

The feasible slot/pole combinations in the proposed machine can be expressed as [21]

$$\begin{cases} N_s = 2mj, \ j = 1, 2, 3\dots \\ N_r = N_s \pm 2k, \ k = 1, 2, 3\dots \end{cases} \quad (5)$$

where m is the phase number. The configurations with odd pole pairs are not employed considering the influence of unbalanced magnetic pull. Meanwhile, based on the flux modulation effect, N_r should be designed in close to N_s to achieve a relatively high pole ratio and torque density. Hence, using a 24-slot stator, four potential slot/pole combinations, 24/20, 24/22, 24/26 and 24/28 are studied in this paper. The slot angle can be expressed as

$$\gamma = \frac{360° N_r}{N_s} \quad (6)$$

With a single-layer concentrated winding design, the electrical angle difference $\Delta\theta_e$ between two adjacent AC armature coils in one phase can be calculated as

$$\Delta\theta_e = (2m\gamma) \bmod (360°) \quad (7)$$

The coil flux phasor diagrams are given in Fig. 11. Considering that phase A consists of coil A1, A2, A3 and A4, the coil flux linkage for A1 can be expanded by Fourier analysis as

$$\varphi_{A1} = \varphi_{dc} + \sum \varphi_n \sin(n\omega t + \theta_n), n = 1, 2, 3\dots \quad (8)$$

where φ_{dc} is the DC flux component, φ_n is the amplitude of the nth harmonics, ω is electrical angular velocity, θ_n is the initial phase angle of the nth harmonics. For 24/20 and 24/28 designs, A1, A2, A3 and A4 have the same flux linkage. Accordingly, phase flux for 24/20 and 24/28 designs can be expressed as

$$\varphi_A = 4\varphi_{A1} = 4\varphi_{dc} + 4\sum \varphi_n \sin(n\omega t + \theta_n), n = 1, 2, 3\dots \quad (9)$$

However, in 24/22 and 24/26 cases, coil flux of A2 and A4, is delayed by 180° than A1 and A3, and thus can be written as

$$\varphi_{A2} = \varphi_{dc} + \sum \varphi_n \sin(n\omega t + n\pi + \theta_n), n = 1, 2, 3\dots \quad (10)$$

The phase flux for 24/22 and 24/26 cases can be expressed as

$$\varphi_A = 2(\varphi_{A1} - \varphi_{A2}) = 4\sum \varphi_n \sin(n\omega t + \theta_n), n = 1, 3, 5\dots \quad (11)$$

It is shown in Equ. (11), in 24/22 and 24/26 cases, the DC bias and all even-order harmonics can be cancelled in the final phase flux, while they are inherited in 24/20 and 24/28 designs. These harmonics are disadvantageous, since they cannot make torque generation but increase core loss and PM eddy current loss.
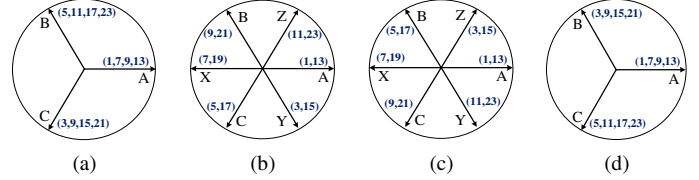

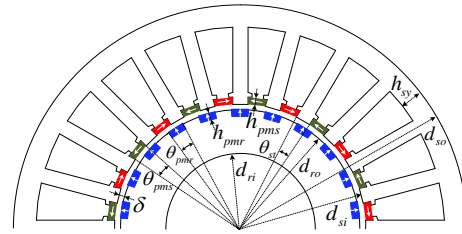Fig. 11. Coil flux phasor diagrams. (a) 24/20. (b) 24/22. (c) 24/26. (d) 24/28.

Fig. 12. General dimension parameters.

TABLE II
Initial Design Parameters of the Proposed 24/22 RDCS-HVM

Symbol	Parameter	Unit	Value
d_{so}	Outer diameter of the stator	mm	120
d_{si}	Inner diameter of the stator	mm	69
d_{ro}	Outer diameter of the rotor	mm	68
d_{ri}	Inner diameter of the rotor	mm	40
δ	Air gap length	mm	0.5
l	Stack length	mm	50
h_{sy}	Height of stator yoke	mm	5
θ_{st}	Arc of stator teeth	°	7
h_{pms}	Height of slot PMs	mm	2
h_{pmr}	Height of rotor PMs	mm	2
θ_{pmr}	Arc of rotor PMs	°	7
	Slot factor	-	0.7
	Wire size (AWG)	-	20
	AC coil number of Turns	-	20
	DC coil number of Turns	-	20

Using finite element method with software Maxwell, the flux characteristic with different slot/pole combinations are assessed. The general dimension parameters are denoted in Fig. 12, with initial design values listed in Table II. Fig. 13 and Fig. 14 shows the calculated no-load flux linkage of two structures, along with harmonic spectrums obtained by Fast Fourier Analysis. It can be found, for both RDCS-RM and CP-VPMM, 24/22 and 24/26 designs can achieve more symmetrical flux linkage with larger fundamental components and reduced even-order components compared with that of 24/20 and 24/28 cases, which agrees with the previous theoretical analysis. The torque performance with different slot/pole combinations is also evaluated. Four variable parameters are optimized to achieve the best toque performance. It can be found from Table III, the 24/22 design has the largest rated torque, minimized cogging torque and torque ripple, thus it is recommended for further investigation.
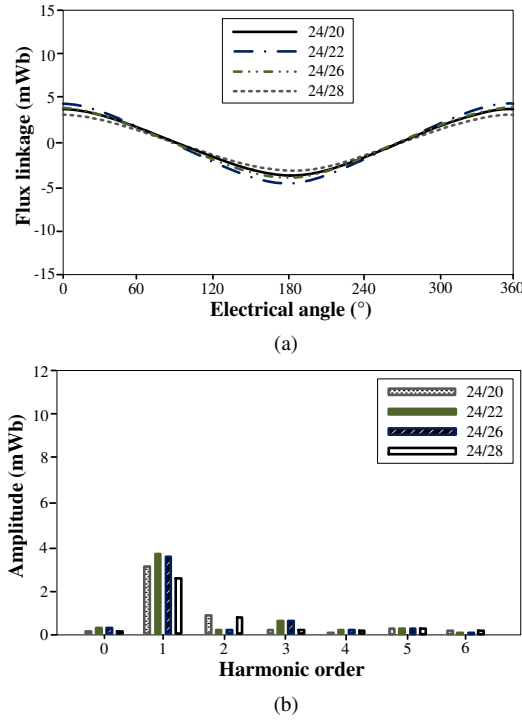
(a)

(b)

Fig. 13. RDCS-RM. (a) No-load phase flux. (b) Harmonics distribution.
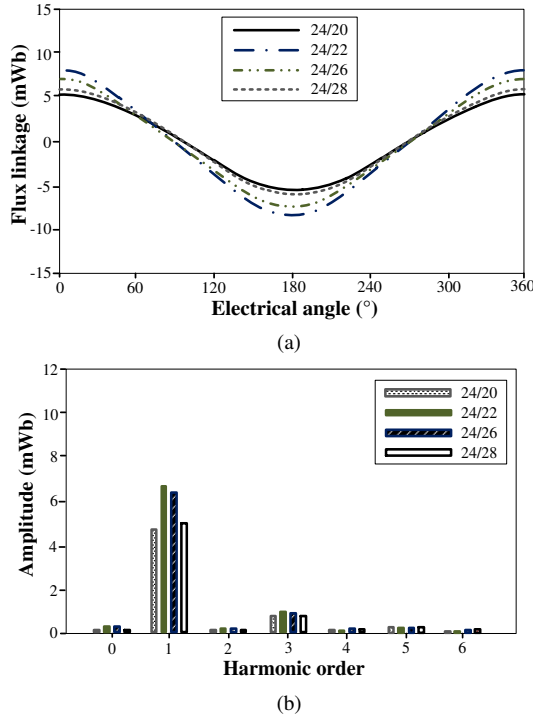

(a)

(b)

Fig. 14. CP-VPMM. (a) No-load phase flux. (b) Harmonics distribution.

TABLE III
Torque Performance with Different Slot/Pole Combinations

N_s	24	24	24	24
N_r	20	22	26	28
θ_{st} (°)	7.2	6.8	6.9	7.1
h_{pms} (mm)	1.7	1.8	2.0	2.1
h_{pmr} (mm)	2.5	2.2	2.5	2.2
θ_{pmr} (°)	8.8	7.8	6.6	6.4
Cogging torque (Nm)	1.42	0.30	0.42	1.63
Torque ripple (Nm)	1.59	0.59	0.76	1.68
Rated torque (Nm)	5.81	7.05	6.64	6.13

V. PERFORMANCE ANALYSIS OF 24/22 DESIGN

In this section, electromagnetic performance of the proposed RDCS-HVM with 24/22 design is evaluated with consideration of different operation modes. Fig. 15 presents the no-load flux distribution at different excitation status. As shown in Fig. 15(a), the flux linkage generated by DC current starts from the wound tooth, enters the rotor salient poles and finally comes back from adjacent stator teeth. This flux linkage contributes to reluctance torque generation. However, it intensifies the level of saturation in stator core. To solve this problem, PMs are introduced into stator slots to produce a constant flux component in stator core, which can be negatively combined with the DC flux bias of DC current. As shown in Fig. 15(b), with the assistance of slot PMs, the flux density in stator core can be greatly reduced, while that in rotor core keeps unchanged almost. In this way, the extra DC saturation effect is relieved, and thus the influence of DC field excitation on PM torque generation of CP-VPMM is minimized. As presented in Fig. 15(c), when DC field current and dual PMs are both active, the flux distribution in stator core mainly arises from rotor PM field, while that in rotor core is a combination of DC field and PM field. This proves the no-load flux linkage in two structures can effectively couple without DC saturation.
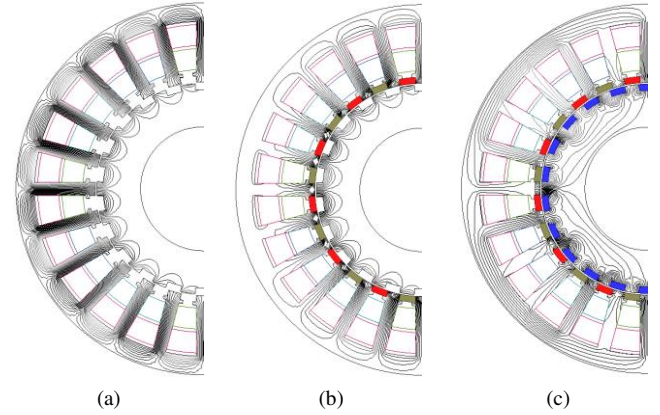

(a)   (b)   (c)

Fig. 15. No-load flux distribution. (a) Only 20A DC current. (b) 20A DC current and slot PMs. (c) 20A DC current and dual PMs.
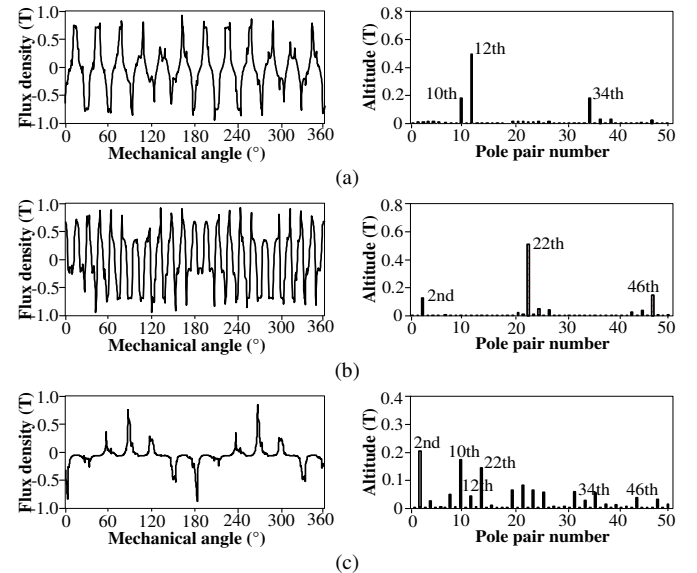

(a)

(b)

(c)

Fig. 16. Flux density in air gap and its harmonics distribution. (a) Only 20A DC field current. (b) Only rotor PMs. (c) Only 20A AC armature current.

Fig. 16 gives the calculated air gap flux density and harmonic distribution excited by different sources. As shown in Fig. 16(a) and Fig. 16(b), those harmonics excited by DC field current and rotor PMs have entirely different pole pair numbers. Therefore, to simultaneously interact with two excitation sources, armature field must be designed with multi working harmonics. Fig. 16(c) presents the air gap field excited by a single-layer concentrated armature winding. It is shown plentiful harmonics are produced by the armature field, and the dominant harmonic components are synchronous with those of two excitation sources. Therefore, it is proved in the proposed machine, single-layer concentrated armature winding can synchronously interact with two hybrid excitation sources benefiting from its harmonic diversity.

Fig. 17 presents the no-load flux linkage. It can be seen, with RDCS-RM and CP-VPMM both active, two flux components can overlap together. Fig.18 shows the torque angle curve with 20A armature current applied. It is shown that reluctance torque in RDCS-RM and PM torque in CP-VPMM can be superposed effectively. Hence, the proposed machine can provide enhanced torque density for HEVs in starting period.
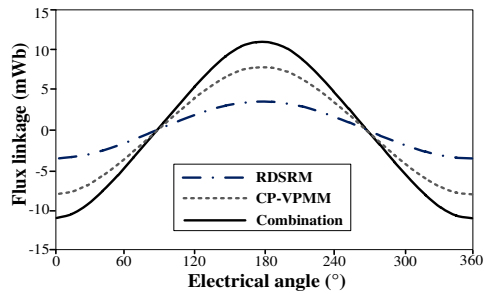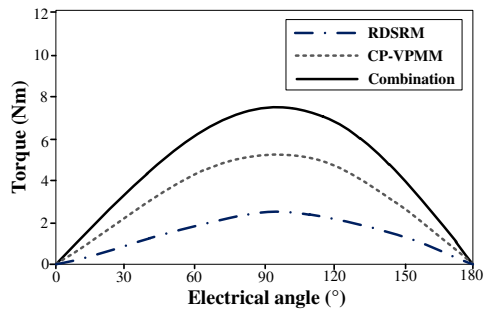

Fig. 17. No-load phase flux linkage.

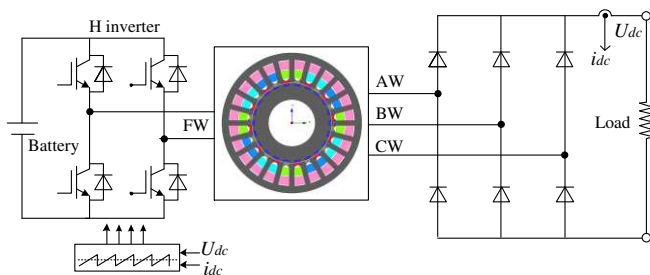Fig. 18. Torque angle curve with 20A AC armature current.

Fig. 19. Field-circuit coupling model for generating operation.

A field-circuit model is built for the proposed RDCS-HVM as presented in Fig. 19 to evaluate its generating performance. The three-phase windings are connected into a passive diode rectifier. DC field current is regulated according to the feedback of output voltage and current. By changing input speed and load resistance, different generation conditions are evaluated.

Fig. 20 presents the no-load phase voltage with bidirectional DC field current. It is shown the phase voltage can be weakened or boosted flexibly. Accordingly, controllable rectified voltage can be obtained at the output terminal as shown in Fig. 21. It is shown, the voltage drop range is larger than voltage boost range, which is caused by inner DC saturation effect. With load current changing, the output voltage characteristic is plotted in Fig. 22. It is revealed DC field current has little influence on the voltage regulation factor. The constant-voltage generation with variable speed is evaluated in Fig. 23. The constant voltage is set at 20V. By regulating DC field current according to load variation, the output voltage can be maintained constant in a wide speed range. As discussed above, the proposed RDCS-HVM is very suitable for the wide-speed on-board generation in HEV.
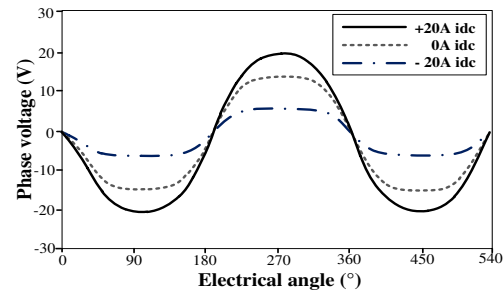

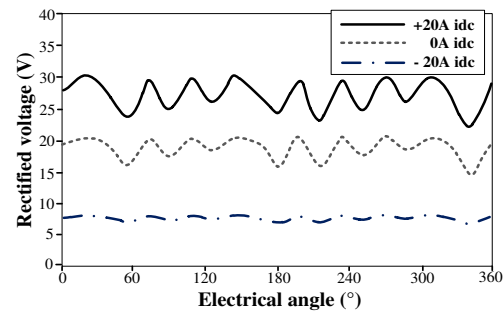Fig. 20. No-load phase voltage at speed 1000 rpm.

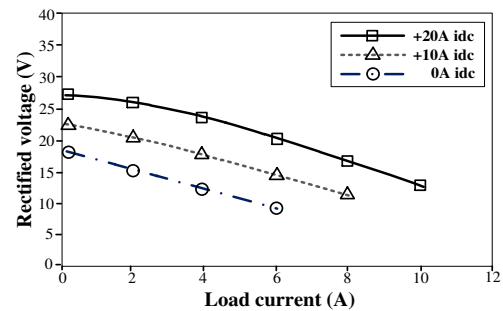Fig. 21. No-load rectified DC voltage at speed 1000 rpm.

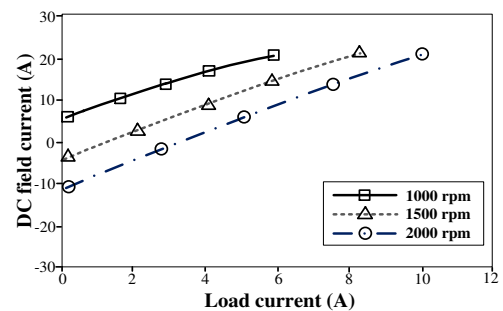Fig. 22. Rectified voltage against load current at speed 1000 rpm.

Fig. 23. DC field current regulation for constant voltage operation.

VI. PARAMETERS ANALYSIS AND DESIGN OPTIMIZATION

A. Dimension Parameters

The influence of important dimension parameters on torque generation in RDCS-HVM is investigated, including the stator yoke height, stator teeth arc, rotor PM height and rotor PM arc. The DC current and AC current are both fixed at 20A.

Fig. 24(a) presents the influence of stator yoke height. It can be noticed, with the increasing of stator yoke height, torque in RDCS-RM and CP-VPMM are almost constant, which means the stator yoke is far from saturated. This is benefiting from the relieving-DC-saturation effect produced by slot PMs.

Fig. 24(b) shows the influence of stator teeth arc. It is found, with the increasing of stator teeth arc, the torque components of RDCS-RM and CP-VPMM are almost unchanged. This means stator teeth arc shows little influence on combined torque.

Fig. 24(c) shows the influence of rotor PM height. With rotor slot height increasing from 1mm to 5mm, the reluctance torque of RDCS-RM shows a distinct increase. This is because RDCS-RM works on the rotor reluctance variation, and the larger rotor PM height is, larger reluctance variation exists. Besides, torque of CP-VPMM keeps increasing until PM height reaches 2mm, and after which it decreases due to the PM saturation effect. The torque combination of RDCSRM and CP-VPMM arrives the saturation point with rotor PM height about 2 mm.

Fig. 24(d) presents the influence of rotor PM arc. The rotor PM height is fixed at 2 mm. With the increasing of rotor PM arc, the reluctance torque of RDCS-RM slightly increases due to the reduced DC leakage flux. The PM torque of CP-VPMM presents a faster growth along with the PM volume increasing. Therefore, to achieve higher combination torque, the rotor PM arc is recommended to be designed relatively larger.

Based on above discussion, it is interesting to find, the torque performance of the proposed RDCS-HVM is more sensitive to rotor dimension parameters than stator dimension parameters, which can be considered during its design optimization.
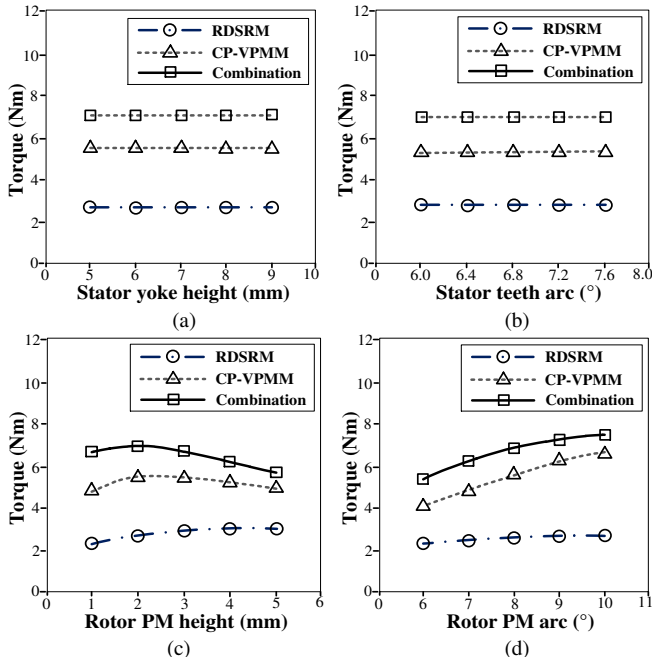
B. AC to DC Split Ratio

In the proposed RDCS-HVM, AC coils and DC coils occupy the same stator slots. It is necessary to investigate the influence of slot split ratio between the AC coils and DC coils on machine performance. As presented in Fig. 25, the reluctance torque of RDCS-RM achieves the maximum value with split ratio of 1: 1, and the combination torque at this point is almost the same as that with the whole AC design. This is because, when split ratio is larger than 1:1, the PM torque trends to be saturated, while the reluctance torque can still make contribution.

Moreover, the voltage regulation ratio is defined as

$$V_r = \frac{e_{idc\_p} - e_{idc\_n}}{e_{idc\_0}} \tag{12}$$

where e_{idc_p}, e_{idc_n}, e_{idc_0} refer to the no-load back EMF values with the positive and negative maximum DC current, as well as zero DC current, respectively. This index represents the control ability of DC field terminal on flux weakening acceleration and constant-voltage generation. It is shown in Fig. 25, with the split ratio increasing, the voltage regulation ratio decreases linearly. With the split ratio of 1:1, the voltage regulation ratio is 84%.

Fig. 26 shows the calculated loss and efficiency performance with different split ratios. It is interesting to found when the split ratio increases, the core loss and PM eddy current loss increases distinctly. This is because the magnetic circuit of CP-PVMM is easier to be saturated than that in RDCS-RM. Consequently, introducing DC field excitation equipped with RDCS effect can relieve the global saturation effect, and further the core loss and PM eddy current loss can be mitigated. In Fig. 26, it can be seen the calculated efficiency with split ratio of 1:1, is higher than that with the whole AC design, which is an inspiring result.

Based on the above analysis, in the proposed RDCS-HVM, the AC to DC slot split ratio is recommended to be 1:1 to obtain good torque performance, optimal voltage regulation, mitigated loss distribution as well as boosted efficiency.
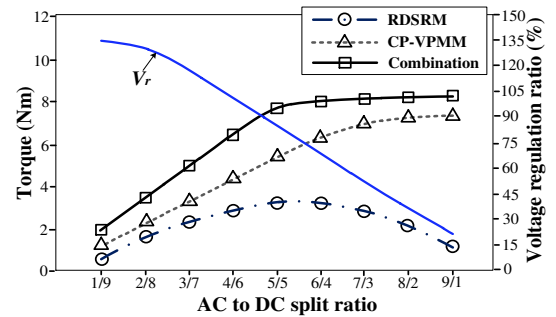

Fig. 24. Influence of dimension parameters on torque performance.

Fig. 25. Influence of AC to DC split ratio on torque and voltage regulation.
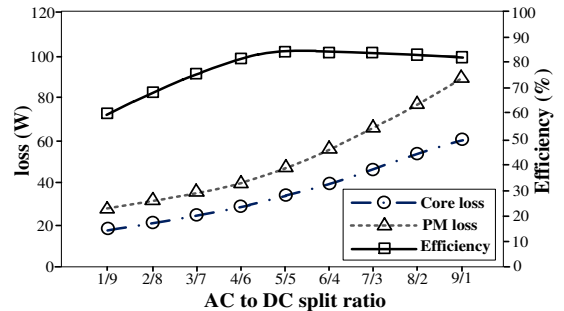

Fig. 26. Influence of AC to DC split ratio on loss and efficiency.

C. Design Optimization

Genetic algorithm (GA), which can search the optimal design by imitating nature selection effect [21], is employed for design optimization of the proposed design. Meanwhile, to reduce time consumption, a two-stage optimization procedure is performed. Specifically, considering the sensitivity of different dimensions parameters, in the first stage all the sensitive design parameters are synchronously optimized by GA with multi objectives, then in the second stage, the best candidate is optimized by involving insensitive parameters individually. The GA optimization flow is presented in Fig. 27. The maximum torque and efficiency are considered as two optimization objectives. Besides, the optimal cases are evaluated by demagnetization analysis at both 200% overload condition and deep flux weakening status. Some final design parameters after optimization and corresponding torque and efficiency performance are presented in Table IV.
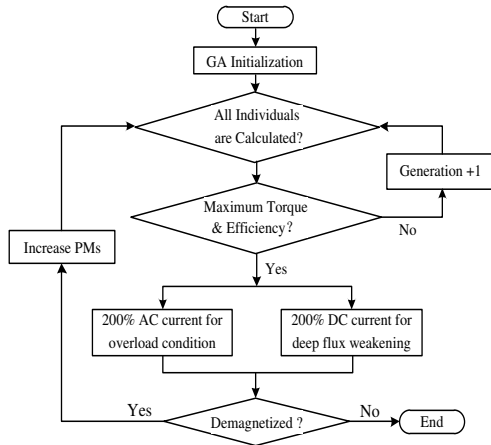

Fig. 27. Optimization flow chart for the proposed machine.

TABLE IV
Some Optimized Parameters and Electromagnetic Performance

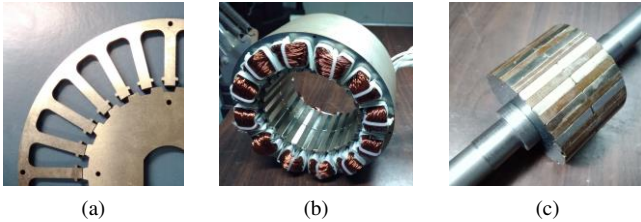| Symbol	Parameter	Unit	Initial	Optimized
h_{sy}	Height of stator yoke	mm	5	5.5
θ_{st}	Arc of stator teeth	°	7	6.8
h_{pms}	Height of slot PMs	mm	2	1.7
h_{pmr}	Height of rotor PMs	mm	2	2.5
θ_{pmr}	Arc of rotor PMs	mm	7	7.9
	Efficiency	%	85	89
	Rated torque	Nm	7.73	8.35

Fig. 28. (a) Lamination steels. (b) Stator assembly. (c) Rotor assembly.

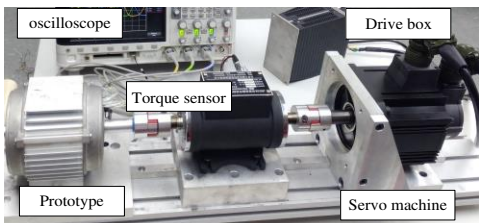Fig. 29. Test platform for the proposed SG system.

TABLE V
Specifications and Materials of the Prototype

Specifications			Materials	
Rated speed	1000 rpm		Type	NdFeB35
Rated voltage	20 V	PMs	Remanence	1.2 T
Rated power	835 W		Coercive force	915 kA/m
Peak Power	1500 W		Type	MG19_24
Phase inductance	0.8 mH	Steel	Saturated point	1.8 T
Phase resistance	0.04 Ω		Mass density	7650 kg/m³

VII. Experimental Verification

To verify the feasibility of the proposed machine, a prototype is manufactured for experimental tests, based on the dimensions in Table II and Table IV. The major specifications and materials are listed in Table V. Fig. 28 shows the details of prototype. To house PMs in slot openings, extra stator pole shoes are designed with stator teeth as shown in Fig. 28(a). The stator assembly is presented in Fig. 28(b). Benefiting from a concentrated design, its wiring process is simple and slot factor is boosted. Fig. 28(c) shows the rotor assembly. Each PM is joint by two segments to reduce eddy current loss. The test platform is shown in Fig. 29, which consists of the prototype, torque sensor, servo machine and drive, DC power source and oscilloscope.
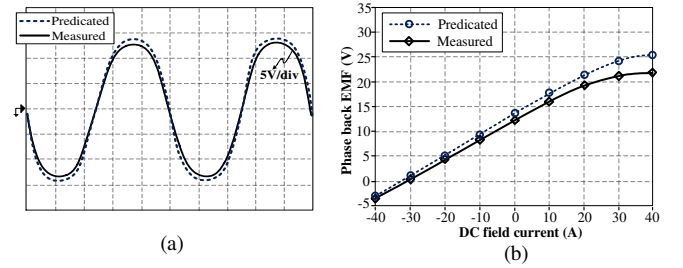

Fig. 30. (a) Phase back EMF at 1000 rpm without DC field current. (b) Phase back EMF with different DC field current.
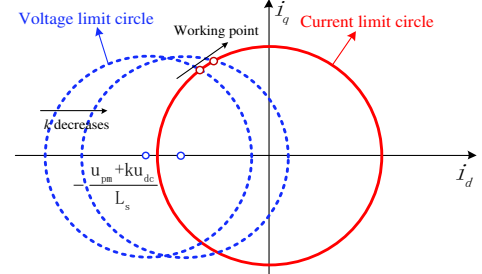
Fig. 31. Variation of current/voltage limits at fixed speed with extra DC control.

Fig. 30 presents the tested phase back EMF at 1000 rpm and its regulation ability with DC current control. It can be seen in Fig. 30(a), the tested back EMF basically agrees with that of the finite element analysis, although its amplitude is a little smaller, which is due to the manufacturing tolerance such as nonuniform PM magnetization level. Fig. 30(b) indicates that the phase back EMF can be bidirectionally regulated by DC field current.

The flux weakening performance is further evaluated for the proposed topology. In the flux weakening operation, the voltage and current limits should be considered as

$$\begin{cases} \left(u_d + u_0 \right)^2 + u_q^2 \le u_{dc}^2 \\ i_d^2 + i_q^2 \le i_{s\max}^2 \end{cases} \quad (13)$$

where u_0 is the no-load back EMF. u_{dc} is the DC bus voltage. $i_{s\max}$ is the inverter current scale. In the proposed RDCS-HVM,

u₀ can be controlled by DC field current, leading to the change of working point during flux weakening as illustrated in Fig. 31. With the extra DC flux weakening effect, reduced i_d current is needed to satisfy the voltage limit, which means under a fixed inverter current scale, larger i_q current can be allowed for torque generation. Therefore, the experiment result in Fig. 32 indicates that larger torque can be produced with extra DC control during flux weakening operation. Consequently, a smaller starting time is consumed with extra DC control as shown in Fig. 33.
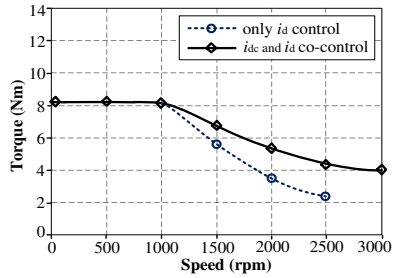

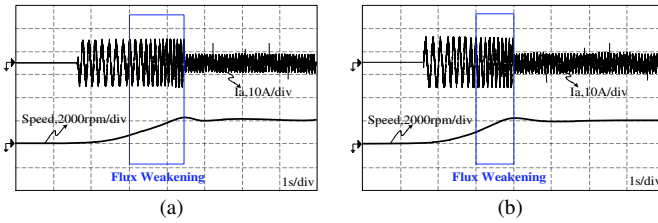Fig. 32. Torque speed curves with different flux weakening controls.

(a) (b)

Fig. 33. Starting performance with load 2Nm. (a) With only id flux weakening. (b) With id and 20A idc combined flux weakening.
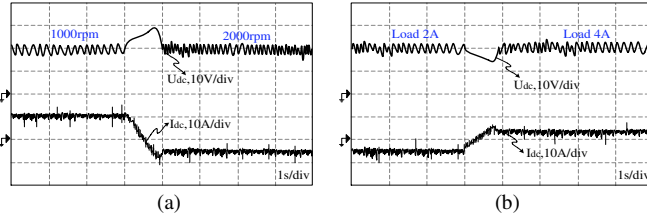

(a) (b)

Fig. 34. Generation performance. (a) Constant load current of 2A, and variable speed from 1000 rpm to 2000 rpm. (b) Constant speed of 1500 rpm, and variable load current from 2A to 4A.
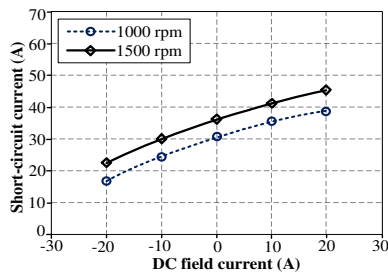

Fig. 35. Short-circuit current with different DC field current.

Fig. 34 shows the measured generating dynamic performance with speed and load changing. It can be found the output voltage can be maintained unchanged by regulating DC field current at different speed and load conditions. The short-circuit current is also measured as shown in Fig. 35. It is revealed that injecting negative DC field current can significantly reduce short-circuit current. This is especially important for safety-critical on-board generation in HEV. In general, the DC field terminal enables a simple and robust generation for the proposed topology.

VIII. COMPARATIVE STUDY

Compared to the traditional CP-VPMM with whole AC coils, in the proposed design, additional DC coils are introduced into stator slots, aiming to utilize the reluctance effect and broaden its application in multi-mode starter generator system. To assess the practicality of this new topology, a feature comparison is performed between the traditional CP-VPMM and the proposed hybrid design, with consideration of the whole speed region in a multi-mode SG system for HEV.

(1) Low-speed constant-torque region. Adopting AC and DC hybrid coils with split ratio 1:1 can achieve comparable torque density to that with the whole AC design, as shown in Fig. 25. There are two reasons for this phenomenon. On one hand, with relieving-DC-saturation design, reluctance torque produced by DC excitation is boosted. On the other hand, PM torque excited by AC excitation is easier to be saturated.

(2) Medium-speed flux weakening region. Introducing extra DC coils in the proposed machine provides an additional flux weakening variable, namely DC current, which can incorporate with d-axis AC current to achieve a combined flux weakening operation. Specifically, using AC and DC hybrid coils with split ratio 1:1 achieves about 84% voltage regulation ratio. This extra magnetization control can relieve the need of d-axis AC current for flux weakening and thus allow larger q-axis AC current for torque generation under a fixed inverter current scale.

(3) High-speed power generation region. With DC field coils in the proposed machine, output voltage can be simply adjusted by DC terminal and a passive rectifier can be adopted for power conversion. This generation system is simpler and more reliable than that for the traditional machine with the whole AC design. Moreover, with extra DC field coils, short-circuit fault becomes bearable in the proposed RDCS-HVM.

Based on the above analysis, it can be concluded, compared to the traditional CP-VPMM with whole AC coils, the proposed RDCS-HVM achieve comparable torque density, boosted flux weakening ability, simpler and more robust power generation, which makes the proposed new topology especially suitable for the multi-mode SG operation in HEVs.

IX. CONCLUSION

This paper presents a relieving-DC-saturation hybrid Vernier machine (RDCS-HVM) as a novel SG candidate for HEVs. The innovation is to introduce the DC field excitation equipped with relieving-DC-saturation effect into the consequent-pole Vernier PM machine (CP-VPMM). And in this way, the advantages of flexible flux control in RDCS reluctance machine and excellent torque density in CP-VPMM are well combined in this topology, making it suitable for the multi-mode SG operation. Especially, boosted reluctance torque and enhanced flux weakening can be achieved during starting period. Meanwhile, the output voltage can be effectively regulated during generation period and short-circuit current is mitigated. In this paper, the proposed machine configuration and its design mechanism are illustrated in detail. Some slot pole combinations are compared, and 24/22 design is recommended for less flux harmonics and smaller torque ripple ratio. Leading design parameters are determined, especially, the slot split ratio is recommended to be 1:1 to achieve both good torque density and wide flux control. Experiment results verify the feasibility of the proposed new topology.

REFERENCE

[1] A. Emadi, Y. J. Lee, and K. Rajashekara, "Power electronics and motor drives in electric, hybrid electric, plug-in hybrid electric vehicles," *IEEE Trans. Ind. Electron.*, vol. 55, no. 6, pp. 2237–2245, Jun. 2008.

[2] L. Chedot, G. Friedrich, J.-M. Biedinger, and P.Macret, "Integrated starter generator: The need for an optimal design and control approach, application to a permanent magnet machine," *IEEE Trans. Ind. Electron.*, vol. 43, no. 2, pp. 551–559, Mar. 2007.

[3] A. Bruyere, and J.C. Mipo, "Modeling and control of a seven-phase claw-pole integrated starter alternator for micro-hybrid automotive applications," in *Proc. IEEE Veh. Power Propulsion Conf.*, pp. 1–6, 2008.

[4] S. Chen, B. Lequesne, R. R. Henry, Y. Xue, and J. J. Ronning, "Design and testing of a belt driven induction starter generator," in *Proc. IEEE IEMDC*, pp. 252–260, 2001.

[5] R. Bojoi, A. Cavagnino, M. Cossale, A. Tenconi, "Multiphase starter generator for a 48-V mini-hybrid powertrain: Design and testing", *IEEE Trans. Ind. Appl.*, vol. 52, no. 2, pp. 1750-1758, Mar. 2016.

[6] A. Tenconi, A. Tenconi and S. Vaschetto, "Experimental characterization of a belt-driven multiphase induction machine for 48-V automotive applications: losses and temperatures assessments", *IEEE Trans. Ind. Appl.*, vol. 52, no. 2, pp. 1321-1330, Mar./Apr. 2016.

[7] R. Bojoi, A. Cavagnino, A. Tenconi and S. Vaschetto, "Control of shaft-line-embedded multiphase starter/generator for aero-Engine," *IEEE Trans. Ind. Electron.*, vol. 63, no. 1, pp. 641-652, Jan. 2016.

[8] C. F. Wang, M. J. Jin, J. X. Shen, and C. Yuan, "A permanent magnet integrated starter generator for electric vehicle onboard range extender application," *IEEE Trans. Magn.*, vol. 48, no.4, pp. 1625–1628, Apr. 2012.

[9] J. Wei, B. Zhou, M. Shi and Y. Liu, "The control strategy of open-winding permanent magnet starter-generator with inverter-rectifier topology," *IEEE Trans. Ind. Inform,* vol. 9, no. 2, pp. 983-991, May 2013.

[10] M. C. Kulan, N. J. Baker, "Design and analysis of compressed windings for a permanent magnet integrated starter generator", *IEEE Trans. Ind. Appl.*, vol. 53, no. 4, pp. 3371-3378, Aug. 2017.

[11] A. V. Radun, C. A. Ferreira and E. Richter, "Two-channel switched reluctance starter/generator results," *IEEE Trans. Ind. Appl.*, vol. 34, no. 5, pp. 1026-1034, Sept.-Oct. 1998.

[12] N. Schofield, and S. Long, "Generator operation of a switched reluctance starter/generator at extended speeds," *IEEE Transactions on vehicular technology*, vol. 58, no. 1, pp. 48-56, 2009.

[13] W. Ding and D. Liang, "A fast analytical model for an integrated switched reluctance starter generator," *IEEE Trans. Energy Convers.*, vol. 25, no. 4, pp. 948–956, Dec. 2010.

[14] S. Ullah, and G. J. Atkinson, "A permanent magnet assist, segmented rotor, switched reluctance drive for fault tolerant aerospace applications," *IEEE Trans on Ind. Appl.*, vol. 55, no. 1, pp. 298-305, Jan.-Feb. 2019.

[15] X. Zhao, S. Niu and W. Fu, "A new modular relieving-DC-saturation Vernier reluctance machine excited by zero sequence current for electric vehicle," IEEE Trans. Magn., vol. 55, no. 7, pp. 1-5, July. 2019.

[16] I. A. Viorel, R. Munteanu, and D. Fodorean, "On the possibility to use a hybrid synchronous machine as an integrated starter-generator," *IEEE International Conference on Industrial Technology*, pp. 1195-1200, 2006.

[17] E. Afjei, H. Toliyat, H. Moradi, "A novel hybrid brushless dc motor/generator for hybrid vehicles applications", *Proc. Int. Conf. Power Electron. Drives Energy Syst.*, pp. 1-6, 2006.

[18] F. G. Capponi, G. De Donato, G. Borocci and F. Caricchi, "Axial-flux hybrid-excitation synchronous machine: analysis design and experimental evaluation", *IEEE Trans. Ind. App.*, vol. 50, no. 5, pp. 31-31, Sep. 2014.

[19] Q. Wang and S. Niu, "Design, modeling, and control of a novel hybrid-excited flux-bidirectional-modulated generator-based wind power generation system," *IEEE Trans. Power Electro.*, vol. 33, no. 4, pp. 3086-3096, April 2018.

[20] X. Zhao, S. Niu and W. Fu, "Design of a novel parallel-hybrid-excited dual-PM machine based on armature harmonics diversity for electric vehicle propulsion," *IEEE Trans. Ind. Electron.*, vol. 66, no. 6, pp. 4209-4219, June 2019.

[21] X. Zhao, S. Niu, "Design and optimization of a novel slot-PM-assisted variable flux reluctance generator for hybrid electric vehicles", *IEEE Trans. Energy Convers.*, vol. 33, no. 4, pp. 2102-2111, Dec. 2018.

[22] H. Yang, Z. Q. Zhu and H. Lin, et al, "Hybrid-excited switched-flux hybrid magnet memory machines," *IEEE Trans. Mag.*, vol. 52, no. 6, pp. 1-15, Jun. 2016.

[23] Q. Wang and S. Niu, "Design optimization of a novel scale-down hybrid-excited dual permanent magnet generator for direct-drive wind power application," *IEEE Trans. Magn.*, vol. 54, no. 3, pp. 1-4, March 2018.

[24] Z. Zhang, Y. Liu and J. Li, "A HESM-Based variable frequency AC starter-generator system for aircraft applications," *IEEE Trans. Energy Convers.*, vol. 33, no. 4, pp. 1998-2006, Dec. 2018.

[25] C. Liu, K. T. Chau, and J. Z. Jiang, "A permanent-magnet hybrid brushless integrated starter–generator for hybrid electric vehicles", *IEEE Trans. Ind. Electron.*, vol. 57, no. 12, pp. 4055-4064, Dec. 2010.

Xing Zhao received the B.Sc. degree in Electrical Engineering from the department of Automation at Nanjing University of Aero & Astro, China, in 2014, and currently he is pursuing Ph.D. degree in Electrical Engineering at the department of Electrical Engineering at the Hong Kong Polytechnic University, Hong Kong. His research interests involve electrical machines and drives.

Shuangxia Niu received the B.Sc. and M.Sc. degrees from Tianjin University, China, in 2002 and 2005, respectively, and the Ph.D. degree from the University of Hong Kong, Hong Kong, in 2009, all in electrical engineering. Currently she is an Associate Professor in the Department of Electrical Engineering at Hong Kong Polytechnic University, Hong Kong. Her researcsssssh interests are electrical machines and renewable energy conversion.

Xiaodong Zhang received the B.Eng. and M.Eng. degrees from the Department of Automation, Tianjin University, China, in 2002 and 2005, respectively. He received the Ph.D. degree in electrical engineering from the Department of Electrical and Electronic Engineering, the University of Hong Kong, Hong Kong, in 2011. His research interests include electric machine design and control.

W.N. Fu received the B.Eng. degree from Hefei University of Technology, Hefei China, in 1982, the M.Eng. degree from Shanghai University of Technology, Shanghai, China, in 1989, and the Ph.D. degree from Hong Kong Polytechnic University, Hong Kong, in 1999, all in electrical engineering. He is currently a Professor at Hong Kong Polytechnic University. Before joining the university in 2007, he was one of the Key Developers at Ansoft Corporation, Pittsburgh, PA, USA. He has about seven years of working experience at Ansoft, focusing on the development of the commercial software Maxwell. His current research interests include electromagnetic field computation, applied electromagnetics, and novel electric machines.